Supporting Information for
Glass-patternable notch-shaped microwave architecture
for on-chip spin detection in biological samples

Keisuke Oshimi,[a,b] Yushi Nishimura,[b,l] Tsutomu Matsubara,[c] Masuaki Tanaka,[d] Eiji Shikoh,[d] Li Zhao,[e] Yajuan Zou,[a,f] Naoki Komatsu,[f] Yuta Ikado,[a] Yuka Takezawa,[g] Eriko Kage-Nakadai,[g] Yumi Izutsu,[h] Katsutoshi Yoshizato,[i] Saho Morita,[j] Masato Tokunaga,[j] HiroshiYukawa,[j,k,l] Yoshinobu Baba,[j,k,l] Yoshio Teki,[b] and Masazumi Fujiwara[a,b]

a. *Department of Chemistry, Graduate School of Natural Science and Technology, Okayama University, Okayama 700-8530, Japan.*
b. *Department of Chemistry, Graduate School of Science, Osaka City University, Osaka 558-8585, Japan*
c. *Department of Anatomy and Regenerative Biology, Graduate School of Medicine, Osaka City University,1-4-3 Asahi-machi, Abeno, Osaka, 545-8585, Japan.*
d. *Department of Electrical and Information Engineering, Graduate School of Engineering, Osaka City University, Osaka 558-8585, Japan.*
e. *State Key Laboratory of Radiation Medicine and Protection, School for Radiological and Interdisciplinary Sciences (RAD-X) and Collaborative Innovation Center of Radiation Medicine of Jiangsu Higher Education Institutions, Soochow University, Suzhou 215123, P. R. China.*
f. *Graduate School of Human and Environmental Studies, Kyoto University, Kyoto 606-8501, Japan.*
g. *Department of Human Life Science, Graduate School of Food and Human Life Science, Osaka City University, Osaka 558-8585, Japan.*
h. *Department of Biology, Faculty of Science, Niigata University, Niigata 950-2181, Japan.*
i. *Synthetic biology laboratory, Graduate school of medicine, Osaka City University, Osaka, 545-8585, Japan.*
j. *Department of Biomolecular Engineering, Graduate School of Engineering, Nagoya University, Nagoya 464-8603, Japan.*
k. *Institute of Nano-Life-Systems, Institutes of Innovation for Future Society, Nagoya University, Nagoya 464-8603, Japan.*
l. *Institute for Quantum Life Science, Quantum Life and Medical Science Directorate, National Institutes for Quantum Science and Technology, Anagawa, Inage-ku, Chiba, 263-8555, Japan.*

I. S-parameter comparison with and without plastic supports (dishes)

(a)

(b)
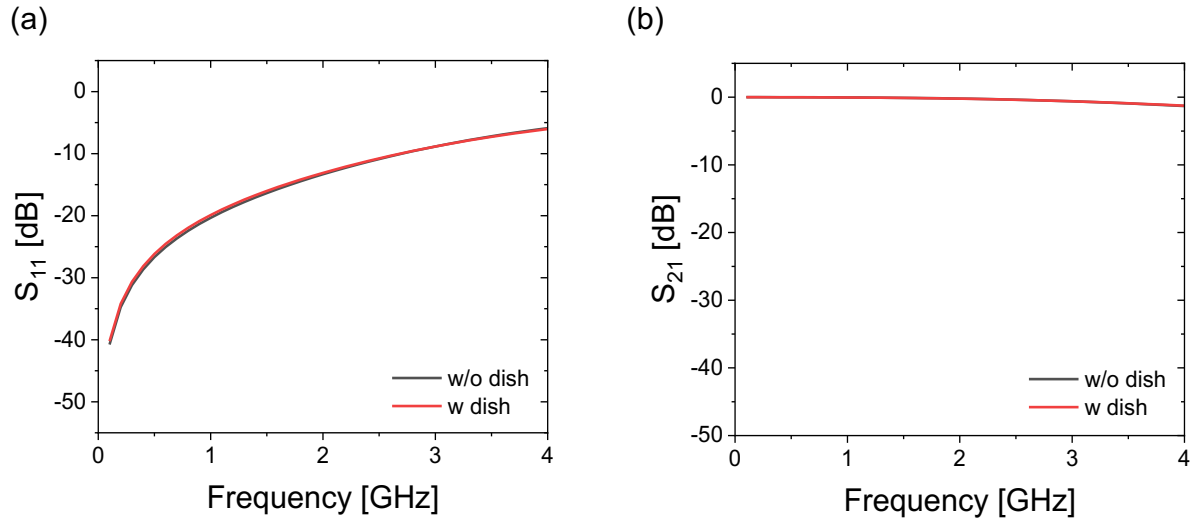
FIG. S1. (a), (b) S-parameter comparison with and without a plastic dish on the chip device.

II.   Convergence of the numerical S-parameter for the different mesh sizes
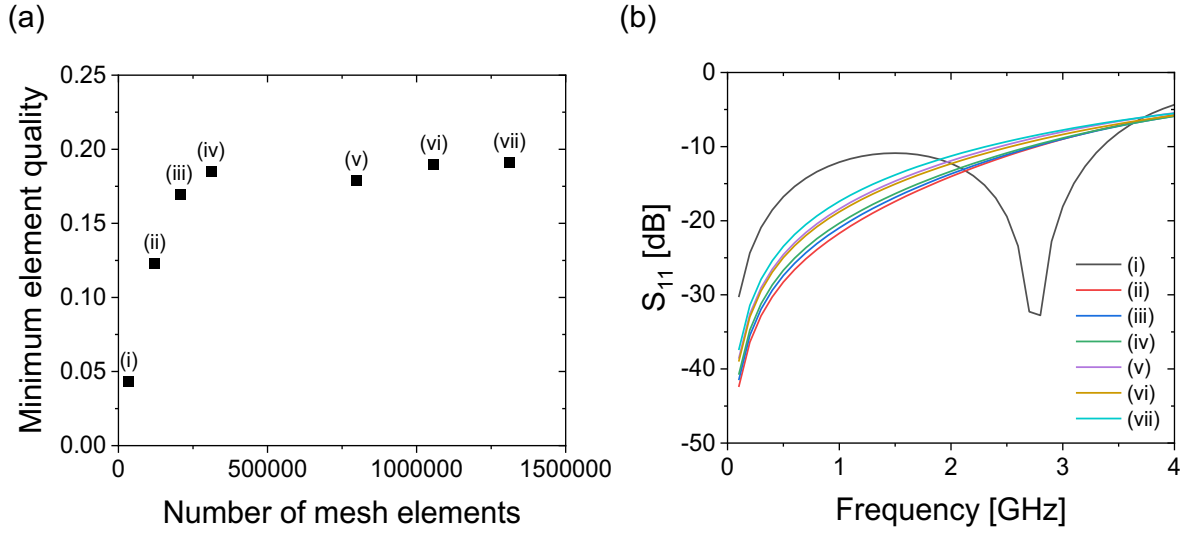
(a)

(b)

FIG. S2. (a) Minimum element quality versus number of mesh elements in the simulations. In COMSOL, condition (i) is called 'extremely coarse', (ii) 'coarse', (iii) 'normal', (iv) 'fine', and (vii) 'extremely fine'. The conditions (v) and (vi) are set to provide intermediates between (iv) and (vii) by varying maximum element growth rate. (b) Convergence of the S_{11} spectrum for different mesh sizes for (i)–(vii). The extremely coarse simulation reveals a peak that disappears with decreasing mesh size, yielding approximately the same S_{11} spectrum.
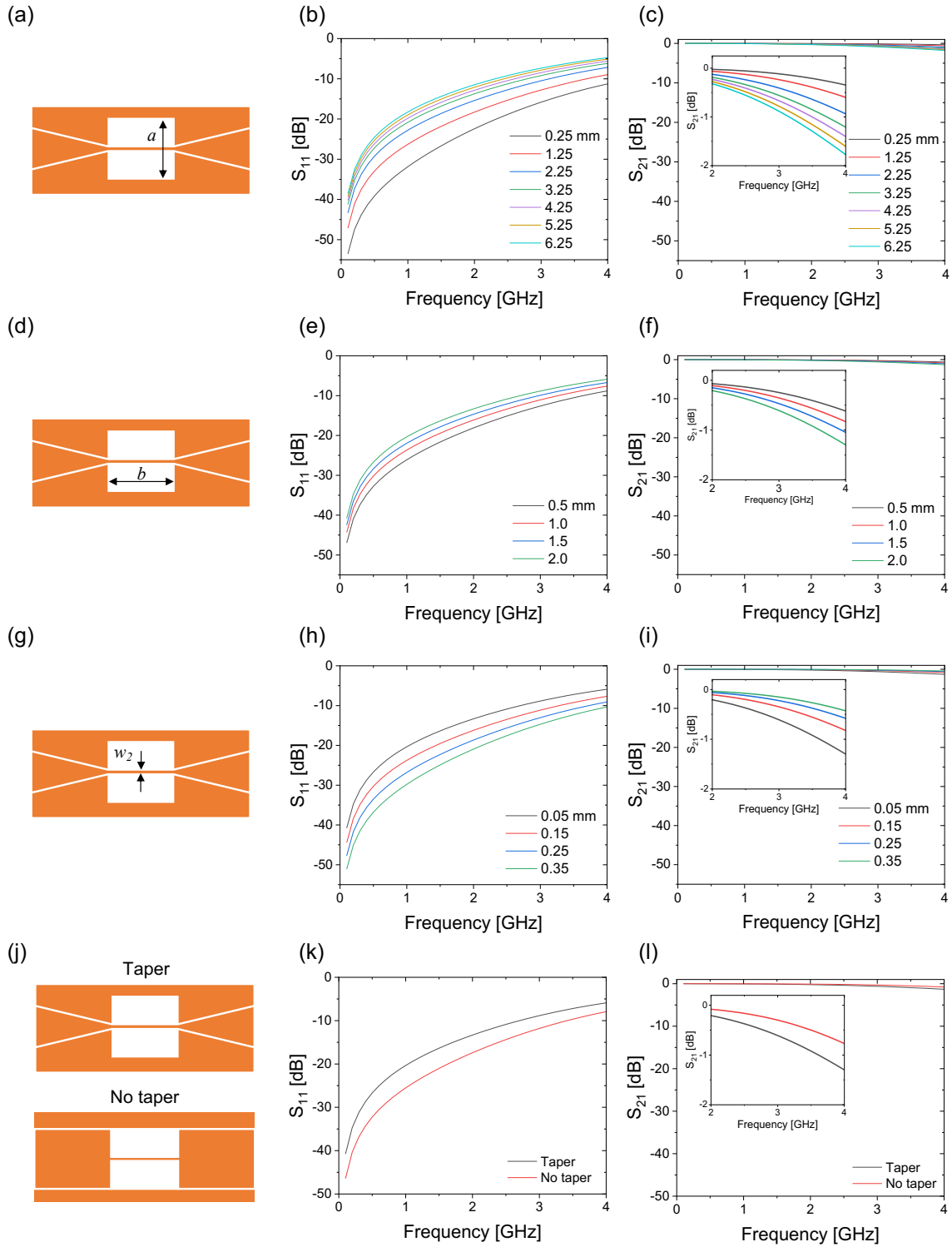
III. Parameter sweeps of the notch shaped antenna

FIG. S3. (a), (b), (c) Schematic diagrams of the notch-shaped geometry, with notch height a and the corresponding S_{11} and S_{21} spectra, respectively. Inset: enlarged S_{21} spectra at 2–4 GHz. (d), (e), (f) Schematic of the notch-shape geometry with a notch width of b and the corresponding S_{11} and S_{21} spectra for different values of b. (g), (h), (i) Schematic of the central thin wire with a width of w_2 in the notch shape and the corresponding S_{11} and S_{21} spectra. (j) Schematics for notch-shape geometry with and without tapers. (k), (l) Simulated S_{11} and S_{21} spectra for taper and no-taper structures.

IV. Comparison of notch shaped antenna with other antenna types on the S-parameters
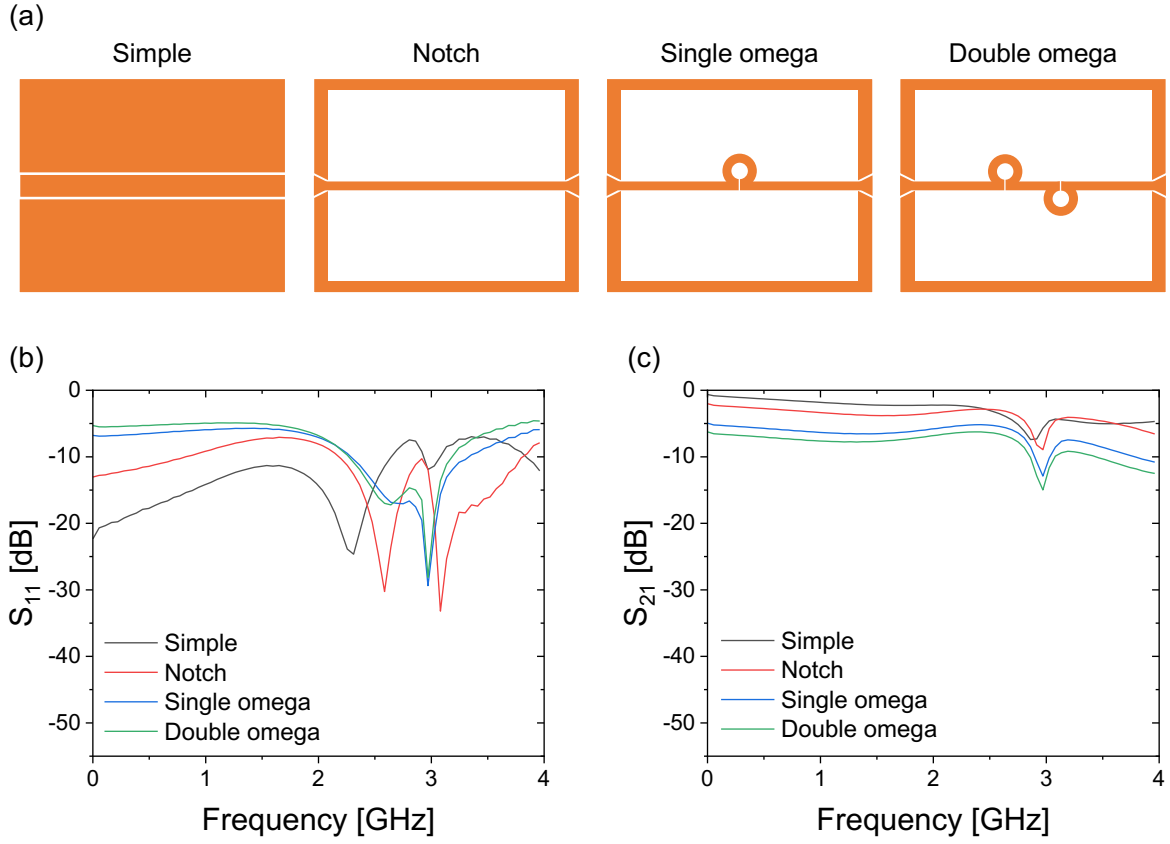

FIG. S4. (a) Schematic drawings for different antenna structures: conventional coplanar (simple), notch (present device), non-resonant single omega (single omega), and non-resonant double omega (double omega). (b), (c) Experimental data of corresponding S-parameter spectra. S_{11} and S_{21} display one or two dips. These dips are absent in the S-parameter simulations (see Fig. 3 in the main text), indicating a cavity resonance by impedance-mismatched reflections at the copper junctions between the coverslip antenna and the PCB.

V. Application to the multi-well dishes and S-parameter characteristics of the conductive rubber connectors
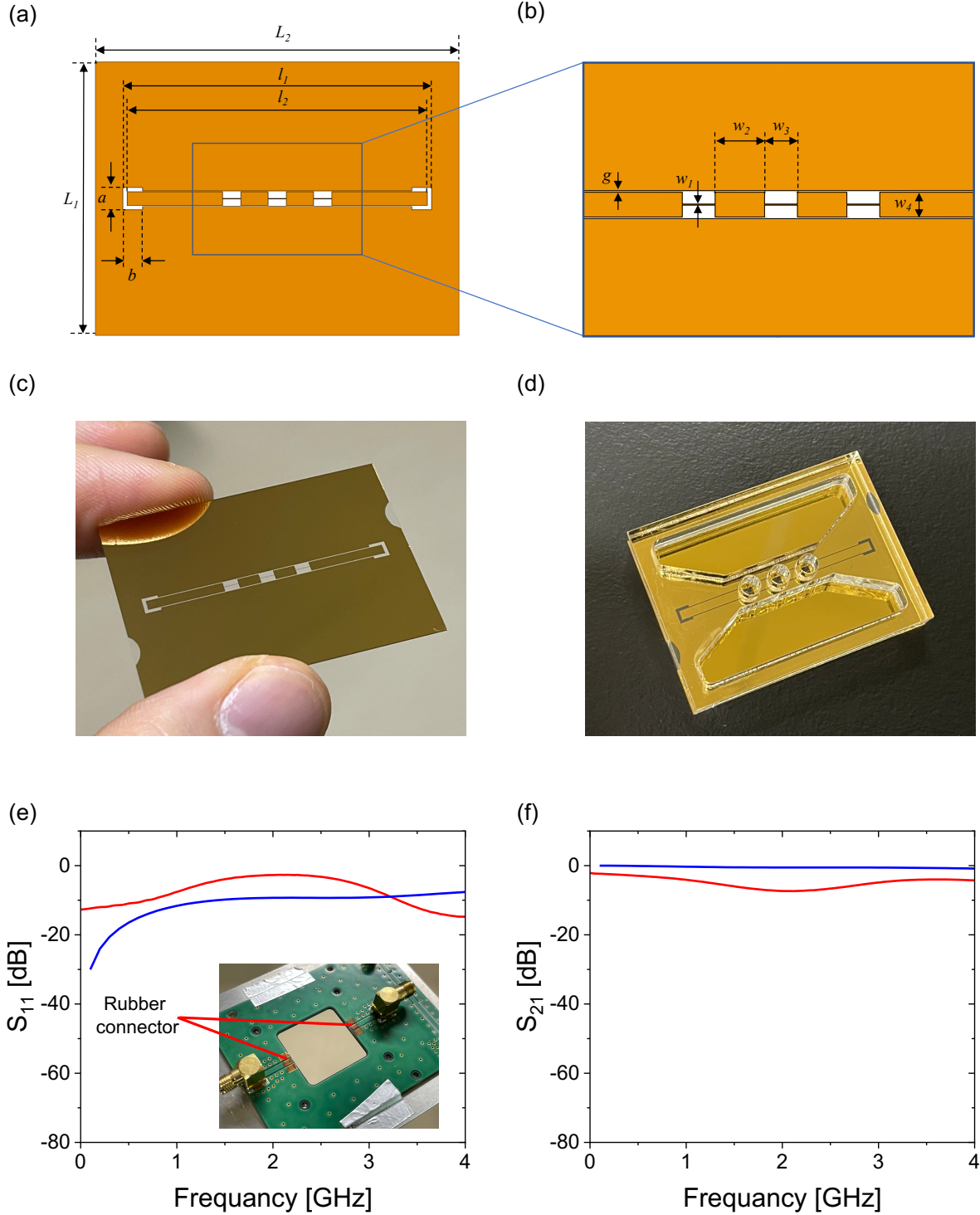

FIG. S5. (a), (b) Geometrical structure of the antenna coverslip for multiwell-dishes with dimensions as follows: $L_1 = 30$ mm, $L_2 = 40$ mm, $l_1 = 33.94$ mm, $l_2 = 33$ mm, $a = 2.44$ mm, $b = 2.17$ mm, $g = 0.1$ mm, $w_1 = 50$ μm, $w_2 = 3.0$ mm, $w_3 = 2.0$ mm, and $w_4 = 1.5$ mm. (c) Photograph of an antenna chip device, comprising three observation areas along the central transmission line. (b) Photograph of a multi-well dish. (d), (e) Experimentally measured (red) and simulated (blue) S_{11} and S_{21} spectra for the multi-well-plate chip device. An anisotropic conductive rubber connector (inset) is used instead of the spring fingers (Fig. 1(b) in the main text) to connect the device to the PCB, in which the finger-derived resonance peaks disappeared.

VI. Microwave system and total gain

Figure S6 shows the schematic diagrams of the present microwave system. Table S1 summarizes the losses and gains of the individual components including SMA cables (taken from their specification sheets) and resultant microwave power. For the amplifier gain, we assumed a minimum gain of 40 dB considering the slight impedance mismatch between the cables and the antenna on PCB. The loss of the copper spring fingers were calculated from S_{11} and S_{21} for the antenna on the PCB as provided in Fig. 3 in the main text. The loss of the incident microwave power at the SMA_1 on the PCB is provided by the following equation [1]:

$$Loss_{in} = 10 \log_{10}(1 - 10^{\frac{S_{11}}{10}}). \tag{1}$$

S_{21} is an indicator related to the microwave transmission on the PCB ($SMA_1 \rightarrow$ antenna $\rightarrow SMA_2$). Therefore, the insertion loss at the first copper fingers (between the SMA_1 and the antenna) is provided by the following equation:

$$Loss_{SMA_1 \rightarrow antenna} = \frac{S_{21}}{2}. \tag{2}$$

A factor of two is determined from the device symmetry. Note that the formulation of Eq. 2 is not affected by losses that we did not explicitly assume as it includes the entire loss from SMA_1 to SMA_2. With these parameters, we find the total irradiation power in the notch shaped area to be 18.9 dBm in the present ODMR experiments (Sec. 3.2, 3.3 in the main text).
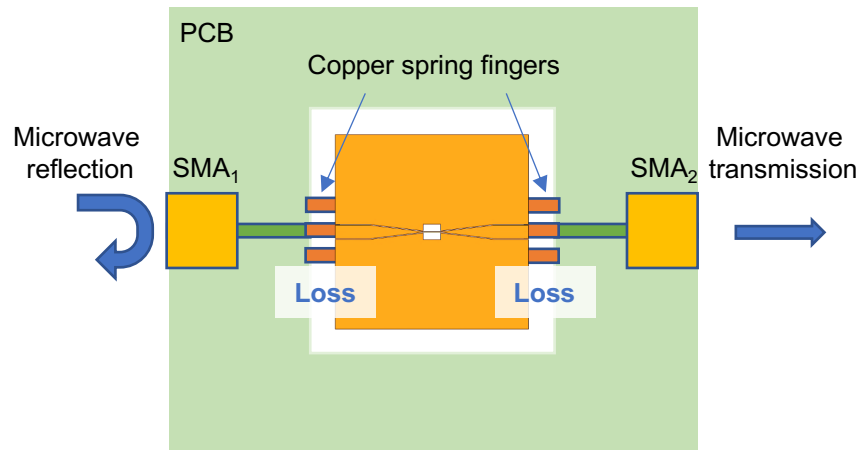
(a)
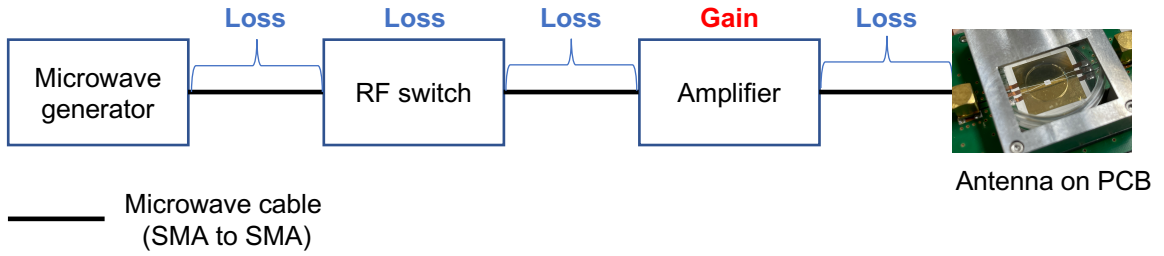
(b)

FIG. S6. (a) Schematic of the microwave system from a microwave generator to an antenna on the PCB in our ODMR experiments. Microwaves are amplified by an amplifier while the microwave loss are caused by the insertion losses of SMA cables and microwave components. (b) Schematic diagram of the microwave reflection and loss on the PCB.

TABLE S1. List of microwave power, loss and gain in the corresponding components. The final power of 18.9 dBm is used for the calculation.

Components	Loss or Gain [dB]	Power [dBm]	Notes
Microwave generator		−7.0	Take from Sec. 3.2, 3.3
RF switches	−3.5	−10.5	Total insertion loss
Microwave amplifier	+40.0	29.5	Amplifier gain
Microwave cables	−7.0	22.5	Total insertion loss
Antenna reflection loss	−0.4	22.1	$S_{11} = -11.0$, using Eq. 1
Antenna insertion loss	−3.2	18.9	$S_{21} = -6.32$, using Eq. 2
Total		18.9 [dBm]	

VII. Theoretical model of ODMR contrast

In Sec. 3.2, we overlaid the theoretical curves of ODMR contrast on the plots of the experimental ODMR. These curves are calculated using the following theoretical equation [2]:

$$C = \Theta \frac{f_R^2}{f_R^2 + \Gamma_p^\infty \Gamma_c^\infty (\frac{s}{1+s})^2}$$
$$f_R = \frac{\gamma |\boldsymbol{B}|}{\sqrt{2}}$$

(3)

where Θ, Γ_p^∞, Γ_c^∞, and s are the overall normalization factor, polarization rate at saturation, rate of optical cycles at saturation, and saturation parameter of the radiative transition, respectively. Here, $\Theta = 0.18$, $\Gamma_p^\infty = 7 \times 10^6$ s^{-1}, and $\Gamma_c^\infty = 9 \times 10^7$ s^{-1} were obtained from Ref. [2]. $s = 0.4$ was determined based on the saturation parameter of the present experimental setup using NA = 0.65 in comparison with that in Ref. [3]. $\gamma = 2.8$ MHz/G is the NV gyromagnetic ratio. For $|\boldsymbol{B}|$, we used simulated $|\boldsymbol{B}|$ generated for the microwave input power defined with a peak voltage of 3.06 V (which effectively corresponds to 18.9 dBm, considering the microwave reflection in the simulation).

Note that $|\boldsymbol{B}|$ in Eq. 3 should take account of the NV axis in a more rigorous manner. f_R should be proportional to the magnetic field perpendicular to the NV axis ($|\boldsymbol{B}|_\perp$) [1, 4, 5], and $|\boldsymbol{B}|$ can be $\frac{|\boldsymbol{B}|_\perp}{\sin\theta}$, where θ is the angle between $\boldsymbol{B}$ (microwave magnetic field) and the NV axis, which we ignored in the present simulation. This discrepancy appears as a relatively large variation of the ODMR depth and Rabi nutation frequency.

VIII. Mcrowave magnetic field near the transmission line

The four Rabi nutation frequency data and the corresponding $|\boldsymbol{B}|$ are summarized in Table S2. These NDs were located at the center close to the transmission line. The distance of NDs from the transmission line are also listed.

TABLE S2. Rabi nutation frequency and $|\boldsymbol{B}|$ near the transmission line

Distance [µm]	f_R [MHz]	$|\boldsymbol{B}|$ [G]
25	3.81	1.93
36	4.53	2.29
44	5.67	2.86
57	3.60	1.82

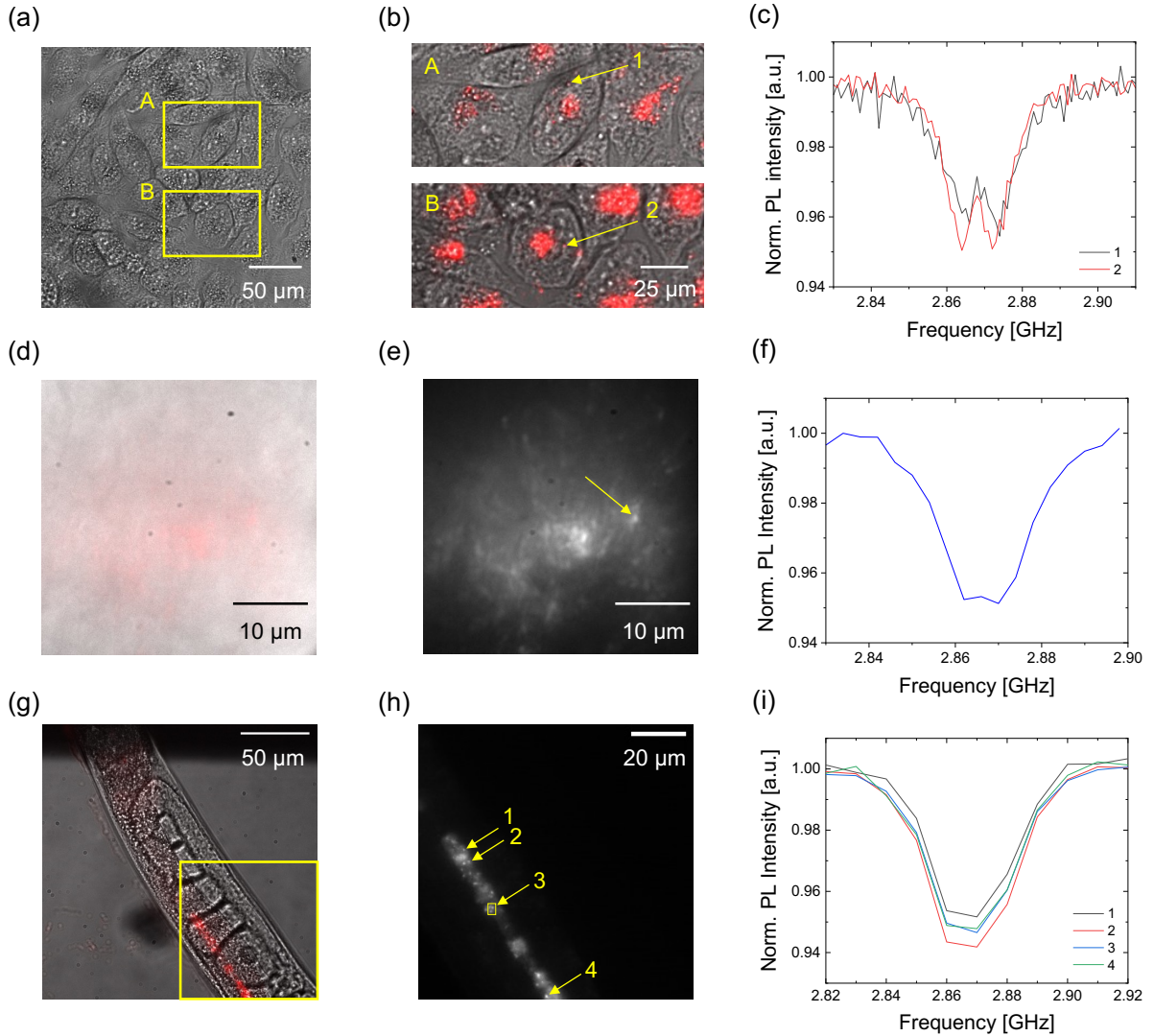## IX. Other data for the biological applications

FIG. S7. (a) Bright-field image of living HeLa cells and (b) merged bright-field images with red fluorescence of ND-labeled HeLa cells inside yellow frames (A and B) in Fig. S7(a). (c) ODMR spectrum of the NDs, indicated by a yellow arrow in Fig. S7(b). The NDs in other cells distributed over $\sim$ 100 µm of the cell in Fig. 6(b) showed comparable ODMR depths. (d) Merged bright-field image of a tissue fragment of the *Xenopus* tadpole tail and (e) red fluorescence image of NDs inside the tissue. (f) ODMR spectrum of the NDs, indicated by a yellow arrow in Fig. S7(e). The NDs in the other tissue from other tadpoles exhibited ODMR depths similar to the data in the main text (Fig. 6(g)). (g) Merged bright-field image of *C. elegans* and (h) red fluorescence image of NDs corresponding to the yellow square in Fig. S7(g). (i) ODMR spectrum of the NDs, indicated by a yellow arrow in Fig. S7(h). NDs distributed over 100 µm in this worm presented ODMR depths within ± 0.01, confirming the $|B|$ uniformity shown in the main text (see Figs. 6 (j)–(l)). Note that the ODMR data for the worm were measured by a camera-based widefield ODMR method, as reported in Ref. [6] (cells and tadpole tissue were measured by the confocal method).

X. Magnetic field distribution of coil and omega shaped antenna
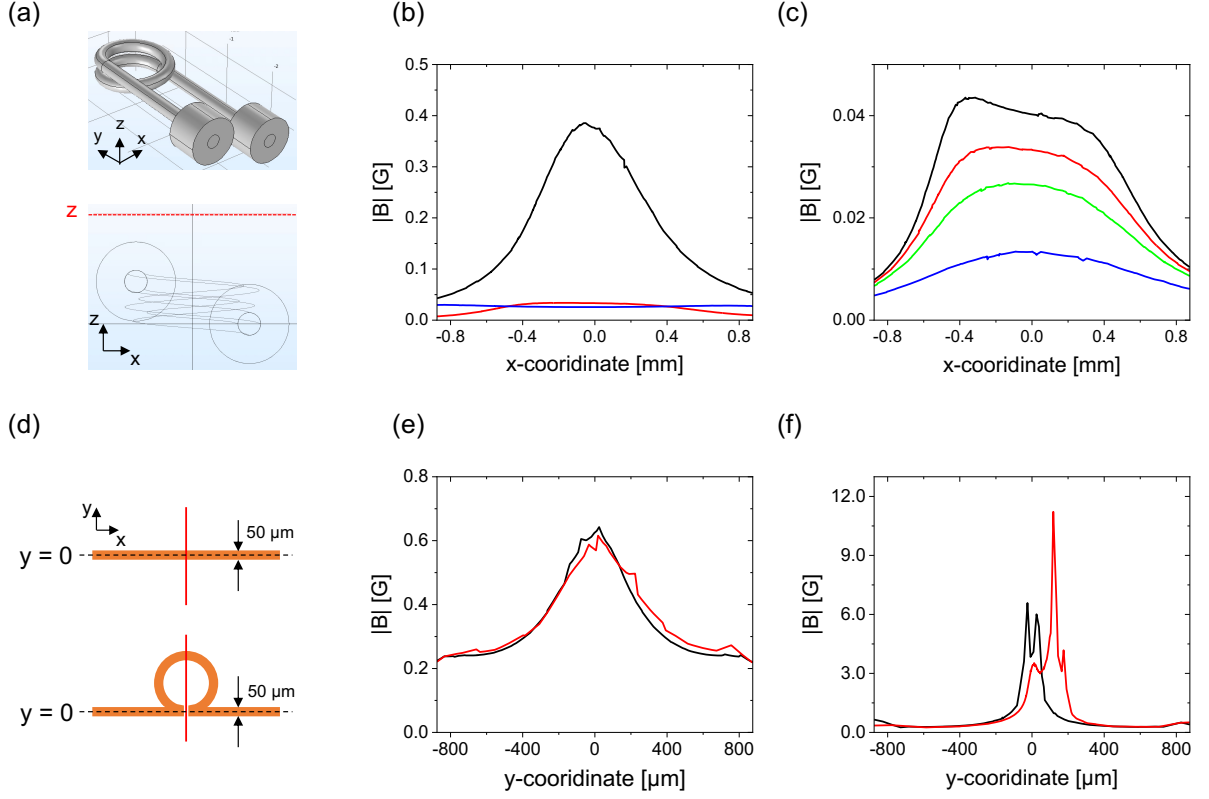
(a)

(b)

(c)

(d)

(e)

(f)

FIG. S8. (a) 3D image of the 1.5-turn coil with the 0.1-mm-diameter wire (upper diagram) and 2D image from y direction (bottom). The dotted line in the z direction identifies the position of the cut for the $|\boldsymbol{B}|$ distribution at $f = 2.87$ GHz and $V = 3.06$ V (peak voltage), as determined by COMSOL. (b) Comparison of the simulated $|\boldsymbol{B}|$ distributions of the coil with diameters of 0.5 mm (black), 1 mm (red), and 2 mm (blue) at $z = 0.17$ mm above the coil. (c) Comparison of the simulated $|\boldsymbol{B}|$ distribution at $z = 0.1$ mm (black), 0.17 mm (red), 0.25 mm (green), and 0.5 mm (blue) above the 1-mm-diameter coil. (d) Images of a straight line (original) and an 100-µm diameter omega-shaped transmission line with our notch antenna. Red lines indicate the cross-section of the $|\boldsymbol{B}|$ distribution; (e) and (f) compare the simulated $|\boldsymbol{B}|$ distribution along the red cross section in Fig. S7(d). The black and red solid lines refer, respectively, to the straight and omega-shaped lines. (e) Results on the surface 0.17 mm (the coverslip thickness) above the antenna plane. (f) Results on the same plane as the antenna.

XI. Live/Dead assay of tissue-derived stem cells (ASCS) on the antenna chip device

(a) Bright field

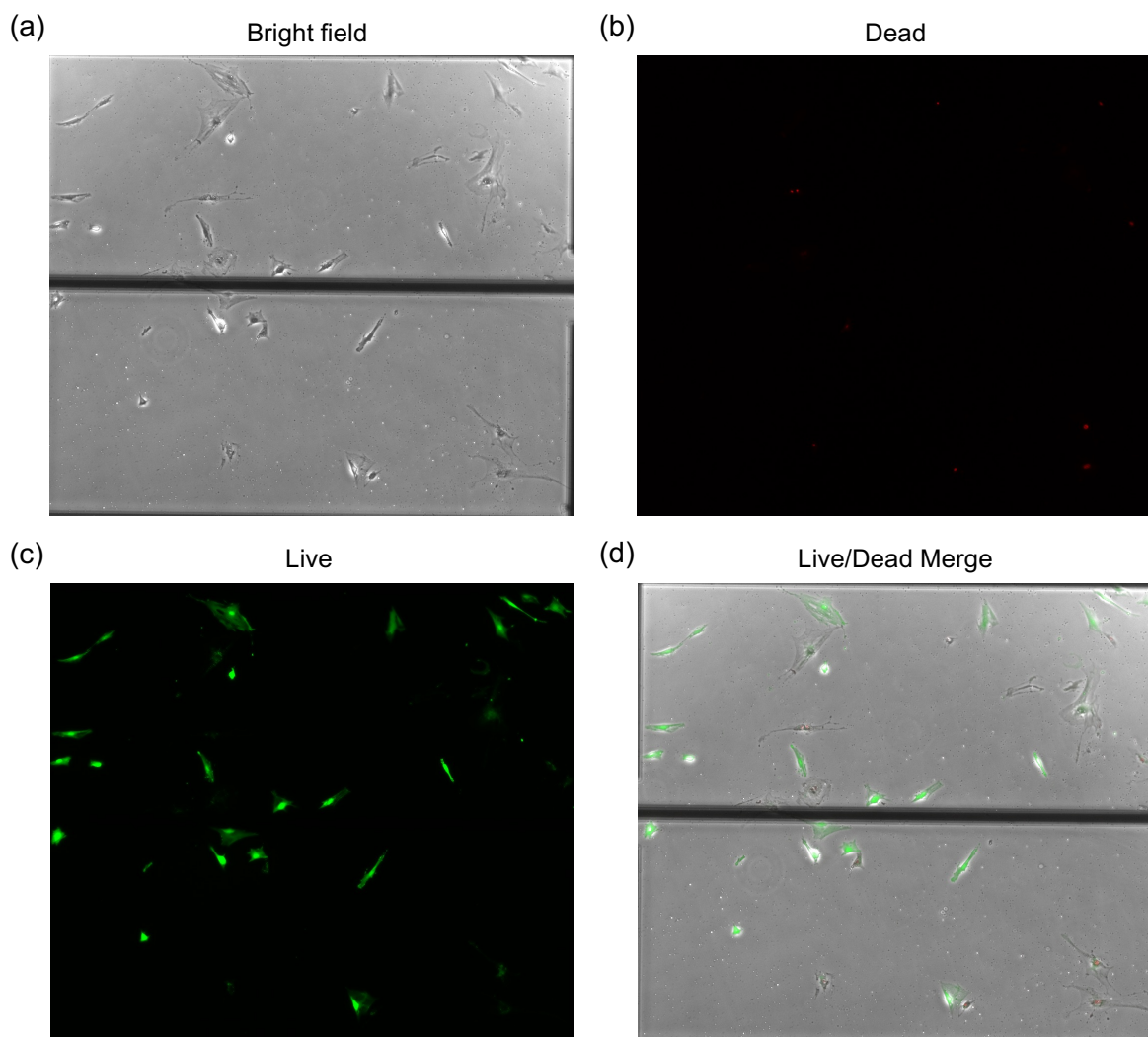(b) Dead

(c) Live

(d) Live/Dead Merge

FIG. S9. (a) Bright-field image of adipose tissue-derived stem cells (ASCs) on the antenna chip device. The central black line shows the thin transmission line of the microwaves. (b) Dead, (c) live stained, and (d) merged images of ASCs on the device, captured using the Live/Dead Viability/Cytotoxicity Kit for mammalian cells (Molecular Probes, L3224). Delicate stem cells such as ASCs can be cultivated in our chip devices.

[1] Hyma H Vallabhapurapu, James P Slack-Smith, Vikas K Sewani, Chris Adambukulam, Andrea Morello, Jarryd J Pla, and Arne Laucht, "Fast coherent control of a nitrogen-vacancy-center spin ensemble using a $KTaO_3$ dielectric resonator at cryogenic temperatures," Phys. Rev. Appl. **16**, 044051 (2021).

[2] A Dréau, M Lesik, L Rondin, P Spinicelli, O Arcizet, J-F Roch, and V Jacques, "Avoiding power broadening in optically detected magnetic resonance of single nv defects for enhanced dc magnetic field sensitivity," Phys. Rev. B **84**, 195204 (2011).

[3] Masazumi Fujiwara, Alexander Dohms, Ken Suto, Yushi Nishimura, Keisuke Oshimi, Yoshio Teki, Kai Cai, Oliver Benson, and Yutaka Shikano, "Real-time estimation of the optically detected magnetic resonance shift in diamond quantum thermometry toward biological applications," Phys. Rev. Res. **2**, 043415 (2020).

[4] R Hanson, VV Dobrovitski, AE Feiguin, O Gywat, and DD Awschalom, "Coherent dynamics of a single spin interacting with an adjustable spin bath," Science **320**, 352–355 (2008).

[5] Kento Sasaki, Yasuaki Monnai, Soya Saijo, Ryushiro Fujita, Hideyuki Watanabe, Junko Ishi-Hayase, Kohei M Itoh, and Eisuke Abe, "Broadband, large-area microwave antenna for optically detected magnetic resonance of nitrogen-vacancy centers in diamond," Rev. Sci. Instrum. **87**, 053904 (2016).

[6] Yushi Nishimura, Keisuke Oshimi, Yumi Umehara, Yuka Kumon, Kazu Miyaji, Hiroshi Yukawa, Yutaka Shikano, Tsutomu Matsubara, Masazumi Fujiwara, Yoshinobu Baba, *et al.*, "Wide-field fluorescent nanodiamond spin measurements toward real-time large-area intracellular thermometry," Sci. Rep. **11**, 1–12 (2021).